

Electronic Supplementary Information

A Thermal Conductive Interface Material with Tremendous and Reversible Surface Adhesion Promises Durable Cross-Interface Heat Conduction

Cong Guo^a, Yuhan Li^b, JianHua Xu^c, Qin Zhang^a, Kai Wu^{*,a} and Qiang Fu^{*,a}

^a College of Polymer Science and Engineering, State Key Laboratory of Polymer Materials Engineering, Sichuan University, Chengdu 610065, P. R. China. E-mails: kaiwu@scu.edu.cn (Kai Wu); qiangfu@scu.edu.cn (Qiang Fu)

^b College of Chemistry and Green Catalysis Center, Zhengzhou Key Laboratory of Elastic Sealing Materials, Zhengzhou University, Zhengzhou 450001, China

^c Joint Laboratory of Advanced Biomedical Materials, College of Chemical Engineering, Nanjing Forestry University, Nanjing 210037, P. R. China.

Experimental Procedures

Effective medium theory model fits the microscopic thermal resistance in PUPDM composites

Table S1 R of PUPDM/ Al_2O_3 composites at different Al_2O_3 contents

Table S2 R of PUPDM/LM/ Al_2O_3 composites at different LM/ Al_2O_3 contents

Details in qualifying the R_c and K_{eff} of the TIM

Fig. S1 Schematic diagram of thermal resistance in series and digital photograph of the sandwiched sample

Results and Discussion

Fig. S2 Synthesis of the inherently adhesive PUPDM

Table S3 Characteristic peak assignments in the Fourier transform infrared spectroscopy of PUPDM

Fig. S3 Characterization of the hierarchical hydrogen bonds in PUPDM

Fig. S4 Lap-shear characterization to qualify the adhesive strength of PUPDM

Table S4 Density information of three components in composites

Fig. S5 Preparation of LM/ Al_2O_3 hybrid filler by grinding LM droplet and Al_2O_3 powder for 60 min

Fig. S6 Characterization of core-shell LM/ Al_2O_3

Fig. S7 Scanning electronic microscopy mapping results of LM/ Al_2O_3 filler with magnification of 250

Fig. S8 Dissolution test of PUPDM in THF

Fig. S9 Frequency sweep of PUPDM at 170 °C

Fig. S10 Statistics of the distance of adjacent fillers and the size of free LM droplets

Fig. S11 Schematic of the PUPDM/LM/ Al_2O_3 composites at a low and a high filler loading

Fig. S12 Synergistic efficiency in the PUPDM/LM/ Al_2O_3 composites

Fig. S13 Average thermal interfacial resistance (R) as a function of the volume fraction of the binary fillers

Fig. S14 Out-of-plane and in-plane thermal conductivity of the PUPDM composites

Fig. S15 The thermal management of a spot-like heat source

Fig. S16 The thermal management of a large-area heat source

Fig. S17 Arrhenius plots at the different temperatures and the activation energy calculation

Fig. S18 Temperature-dependent Fourier transform infrared spectrum of the PUPDM/LM/ Al_2O_3 composite

Fig. S19 Lap-shear strength of PUPDM composites

Fig. S20 Temperature dependence of lap-shear strength of PUPDM/LM/ Al_2O_3 composite

Fig. S21 Corrosion of aluminum surface after contacting with PUPDM/LM/ Al_2O_3 and LM verse time

Fig. S22 SEM images and Energy-dispersive spectra results of different aluminum surfaces

Fig. S23 Interfacial thermal management for rough substrates

Table S5 Comparison of thermal contact resistance (two sides) of PUPDM/LM/ Al_2O_3 composite TIM with those of reported TIMs

References

Experimental Procedures

Materials

Polytetramethylene ether glycol (PTMEG, $M_n = 1000$ g/mol, $f = 2$), dibutyltin dilaurate (DBTDL), and N, N-Dimethylformamide (DMF) were offered by Aladdin. Isophorone diisocyanate (IPDI) was supplied by Adamas. 2, 6-pyridinedimethanol (PDM) was purchased from Shanghai Bide Technology Co., Ltd. The chemical reagents mentioned above were used without further purification. Toluene and tetrahydrofuran (THF) were supplied by Sinopharm Chemical Reagent Co., Ltd, and utilized after distillation. Zhenjiang Fanyada Electronic Technology Co., Ltd offered gallium-indium-tin liquid metal. Spherical aluminum oxide (diameter of ≈ 20 μm) was provided by Suzhou Jinyi New Materials Technology Co., Ltd. Commercial thermal silicon pads (4 W m/K) were offered by Shenzhen Pinshuo Electronic Materials Co., Ltd.

Synthesis of reversibly adhesive PUPDM

We synthesize the PUPDM with $[\text{NCO}]/[\text{OH}]$ value of 2.7 (the value is defined as a molar ratio of isocyanate groups to hydroxyl groups of PTMEG) through the following procedures. First, to remove residual moisture, PTMEG (20 g, 20 mmol) was added in a dried glass vessel equipped with a mechanical stirrer. It was heated by an electrical heating jacket at 120 °C under vacuum for 1 h. After cooling down to 80 °C, IPDI (12 g, 54 mmol, $[\text{NCO}]/[\text{OH}] = 2.7$) was added into the vessel and stirred for 1 h under argon atmosphere. Then, catalyst DBTAL (2.53 mg, 4×10^{-3} mmol) was dissolved in anhydrous toluene and added into the above system. The chemical reaction continues for another 3 h. Afterward, anhydrous toluene was added to adjust the viscosity, followed by employing PDM power (4.73 g, 34 mmol) as the chain extender to the system to complete the reaction at 80 °C. It took about 10 h until the NCO peak in the FTIR spectrum disappeared. Finally, the mixture in the vessel was transferred into a rectangular mold and brought to vaporize the solvent in a fume hood at ambient conditions for 24 h. The product was dried at 80 °C for another 24 h in an air-circulating oven, followed by removing residual solvent at 80 °C for 24 h in a vacuum oven.

Fabrication of LM/Al₂O₃ hybrid filler

A certain amount of LM and Al₂O₃ were put in an agate mortar. Then, the LM/Al₂O₃ binary filler was fabricated by solid grinding the mixtures for approximately 60 min until the color of the hybrid filler was uniform, ensuring the maximal interaction and reaction between LM and Al₂O₃.

Fabrication of PUPDM/LM/Al₂O₃ composites

First, 10 g PUPDM was dissolved in 23.33 g DMF under magnetic stirring at 80 °C for 4 h to form a homogeneous PUPDM solution. Then, we adequately mixed the suitable amount of LM/Al₂O₃ powder with the solution using a pestle to grind in a mortar for 10 min. Subsequently, the mixture undergoes shear-induced turbulent flow for 10 min until obtaining a homogeneous viscous suspension. Afterward, the composites solution was co-precipitated in deionized water. Last, the collected precipitates were dried in a vacuum oven to remove residual solvent at 80 °C for 48 h and then processed into the desired shape by hot press molding at 150 °C. PUPDM/LM and PUPDM/Al₂O₃ composites were fabricated via identical processes.

Characterization

¹H NMR (d-THF) analysis was performed on a nuclear magnetic resonance (NMR) spectrometer (Bruker Avance 400 MHz, Germany). FTIR spectra and variable-temperature FTIR spectroscopy were performed on a Nicolet 6700 (Thermo Electron Corporation, USA), and the temperature was set to rise from 25 °C to 125 °C with 10 °C interval. 2D correlation spectroscopy was carried out based on variable-temperature FTIR spectra and calculated via the software (2DCS Professional I-002). TA instrument DSC-25 was utilized for the DSC experiments at a 5 °C/min heating rate under a nitrogen atmosphere. GPC (HLC-8320, Japan) equipped with a tetrahydrofuran column was used to obtain the molecular weight information. XRD patterns were conducted with a Rigaku Ultima IV diffractometer (Cu K_α radiation, $\lambda = 0.15406$ nm) to analyze lattice distortion of Al₂O₃ after being modified by LM at a scanning rate of 2 °/min. In-plane and out-of-plane thermal conductivity can be calculated by the equation $\kappa = \alpha \times \rho \times C_p$, where α is the thermal diffusivity, ρ is the sample density, and C_p is the specific heat capacity. Laser flash analysis (LFA467, Netzsch, Germany) was used to measure α of samples. Their double sides were sprayed with graphite before the measurements to guarantee the identical absorption of laser energy, and C_p can be determined by DSC (STA 449F3, Germany) with sapphire as the standard sample. C_p of the composite can be calculated by the equation $C_{p-composite} = C_{p-A} \varphi + C_{p-B} (1-\varphi)$, where C_{p-A} is the specific heat capacity of constituent A, C_{p-B} is the specific heat capacity of constituent B, and φ is the mass ratio of constituent A. The sample density (ρ) was measured by using the Archimedes method (JA203 Puchun Instruments, China). Thermogravimetric analysis (TGA 55, TA, USA) was carried out to verify the volume fraction of LM/Al₂O₃ binary filler within the composites. The filler morphological images, cross-sectional views of composites, sandwiched interfaces, and the corresponding elemental mapping results were

obtained via high-resolution field emission SEM (Apreo S, USA) equipped with an electron backscatter diffractometer (EBSD). All infrared images were obtained using an infrared camera (FLIR-T600) to record the temperature distribution of the samples. Rheological tests were conducted on a rheometer (MCR-302, Anton-Paar, Austria) using a 25 mm-diameter parallel steel plate. Temperature sweeps were carried out at a frequency of 1 Hz and a strain of 0.5 % in a temperature range from 25 °C to 150 °C, and the stress relaxation experiments were performed in a constant strain of 1%. Frequency sweep was performed at the strain of 0.5 % and the frequency range is from 360 to 1 rad/s. Mechanical lap-shear testing was conducted on a universal tester (Instron 5967, USA) with a 100 mm min⁻¹ strain rate. The samples were sandwiched between two pieces of substrates and placed in an oven at a set temperature under a preload of about 100 kPa, followed by cooling down to room temperature before the lap-shear testing. The preload was removed during the lap-shear testing.

Effective medium theory model fits the microscopic thermal resistance in PUPDM composites

The microscopic interfacial thermal resistance (R) is quantified according to the effective medium theory model, in which synthesized PUPDM is taken as the matrix, and thermally conductive Al_2O_3 or LM/ Al_2O_3 hybrid filler is considered as the additive. Its value is calculated according to following equation S1:

$$\kappa_e = \frac{f\kappa_c}{p + \frac{1-f}{D}\frac{\kappa_c}{\kappa_m}} \quad (\text{S1})$$

where κ_e is the κ of PUPDM composites material, κ_m is the κ of PUPDM matrix, f is the volume content, p is the aspect ratio, D is the diameter. For PUPDM/ Al_2O_3 composites, κ_m is characterized as 0.221 W/m K, p is valued as 1 because of the spherical shape, D is averaged as 21.140 μm according to the SEM observation, and κ_c is 30 W/m K for pristine Al_2O_3 . Therefore, R is calculated based on above parameters and the results are provided in Table S1.

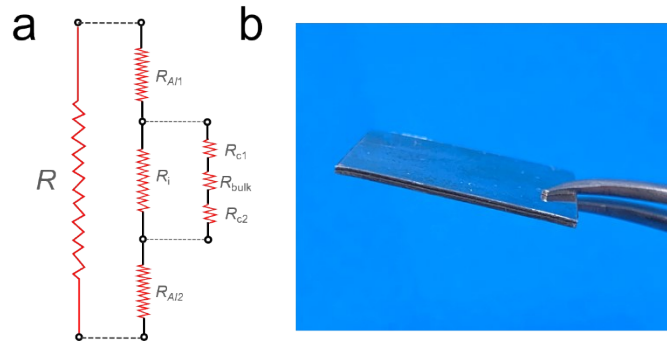
Table S1 R of PUPDM/ Al_2O_3 composites at different Al_2O_3 contents.

f (%)	11.76	23.00	33.96	44.40	54.55	64.30	73.68	82.76
R ($10^{-7} \text{ m}^2 \text{ K W}^{-1}$)	37.10	19.30	20.00	13.00	7.53	6.12	6.72	7.44

For PUPDM/ Al_2O_3 /LM composites, κ_m is still valued as 0.221 W/m K, p is valued as 1 because of the estimated spherical shape of hybrid filler, D is averaged according to the SEM observation and the equation ($D_{\text{Al}_2\text{O}_3/\text{LM}} = D_{\text{Al}_2\text{O}_3}f_{\text{Al}_2\text{O}_3} + D_{\text{LM}}f_{\text{LM}}$), and κ_c of Al_2O_3 /LM hybrid filler is calculated as 29.530 W/m K according to the parallel model ($\kappa_c = f_{\text{Al}_2\text{O}_3}\kappa_{\text{Al}_2\text{O}_3} + f_{\text{LM}}\kappa_{\text{LM}}$). The calculated R is provided in Table S2.

Table S2 R of PUPDM/ Al_2O_3 /LM composites at different Al_2O_3 /LM contents.

f (%)	11.76	23.00	33.96	44.40	54.55	64.30	73.68	82.76
R ($10^{-7} \text{ m}^2 \text{ K W}^{-1}$)	24.77	21.64	17.21	12.32	7.88	5.24	2.34	1.17



Details in qualifying the R_c and κ_{eff} of the TIM

Fig. S1 (a) Schematic diagram of thermal resistance in series. (b) Digital photograph of the sandwiched sample.

R_c and κ_{eff} of the TIM can be calculated by the following equation S2-S5:

$$R = R_{Al} + R_i \quad (S2)$$

$$R_i = R_{bulk} + R_c = BLT/\kappa_{eff} \quad (S3)$$

$$R_{bulk} = BLT/\kappa_{TIM} \quad (S4)$$

$$R_c = R_{c1} + R_{c2} \quad (S5)$$

where R is the total thermal resistance of the sandwiched thermal interface, R_{Al} is the thermal resistance of aluminum plates at the hot side and cold side, R_i is the total resistance of the interface between two aluminum plates, R_{bulk} is the intrinsic thermal resistance of the TIM, R_c is the thermal contact resistance between the TIM and the double sides, BLT is the bond line thickness, κ_{eff} is the effective thermal conductivity of a TIM, κ_{TIM} is the intrinsic thermal conductivity of a TIM.

Firstly, before thermal properties measurements, the samples were sandwiched between two pieces of aluminum plates and placed in an oven at a preset adhesion temperature under a preload of about 100 kPa, followed by cooling down to room temperature. Then, the preload was removed during the measurements to obtain R_c under zero pressure. The thermal conductivity of single aluminum plate and the sandwiched thermal interface were all measured through laser flash analysis. BLT was obtained by subtracting the thickness of two aluminum plates from the total thickness of sandwiched thermal interface.

Results and Discussion

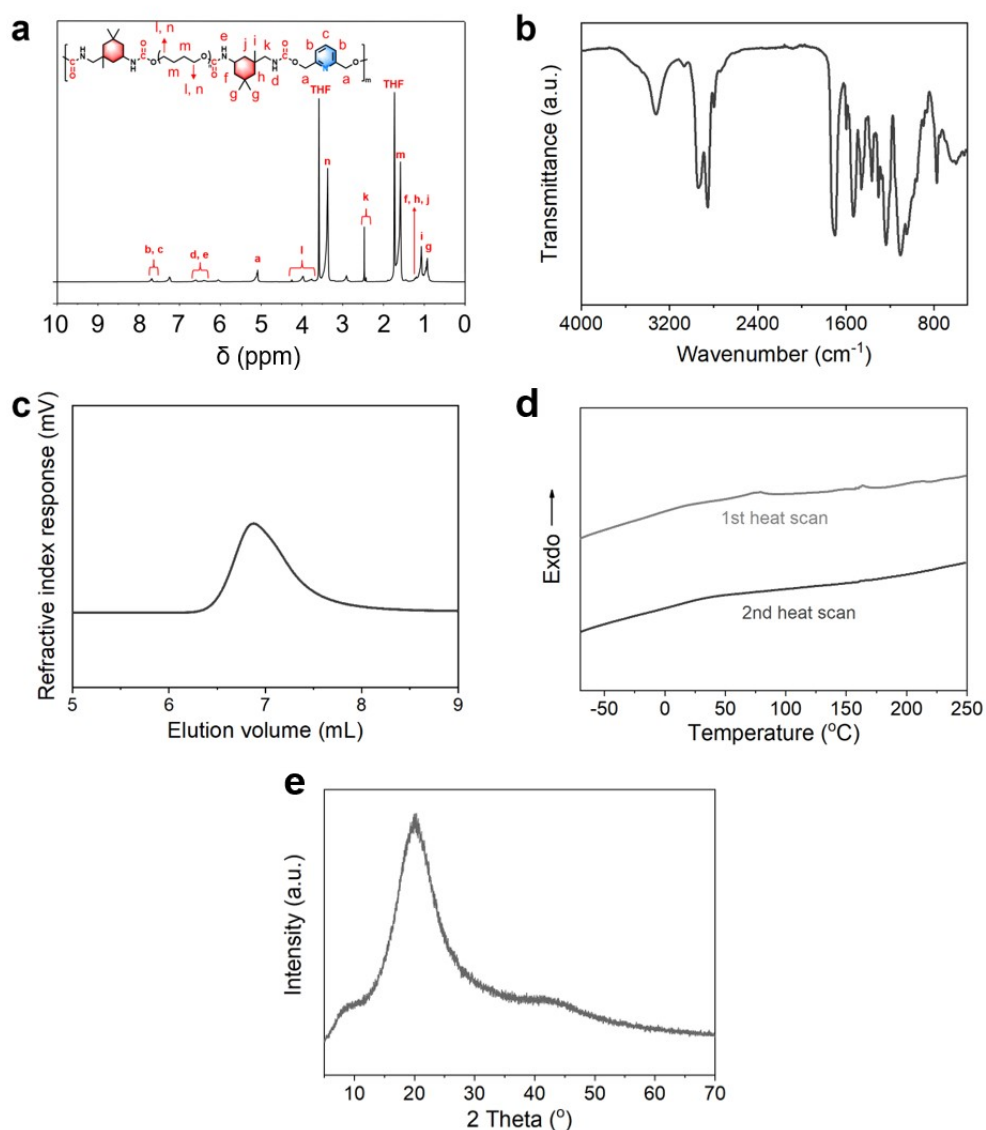


Fig. S2 Synthesis of the inherently adhesive PUPDM. (a) ^1H nuclear magnetic resonance chemical shift of PUPDM. (b) Fourier transform infrared spectroscopy of PUPDM. (c) Tetrahydrofuran-based gel permeation chromatography profiles of PUPDM, with M_n of 41130 g/mol, M_w of 69707 g/mol, and polydispersity index of 1.695. (d) Differential scanning calorimetry curve of PUPDM with temperature increasing from -60 to 250 °C. (e) XRD curve of PUPDM.

As shown in Fig. S2d, small melting peak could be found from 1st heat scan and the peak disappears from 2nd heat scan. Combined with the XRD curve of PUPDM displaying a broad diffraction peak centered at $2\theta=20.1^\circ$ with FWHM of 8.97° , it could be concluded that very small amounts of crystalline domains exist in PUPDM elastomer but crystallization kinetics is slow.

Table S3 Characteristic peak assignments in the Fourier transform infrared spectroscopy of PUPDM.

Wavenumber (cm ⁻¹)	Assignments
3450	free <i>n</i> (NH)
3324	H-bonded <i>n</i> (NH)
2939	<i>n_a</i> (CH ₂)
2915	<i>n_a</i> (CH ₂)
2855	<i>n_s</i> (CH ₂)
2795	<i>n_s</i> (CH ₂)
1717	free <i>n</i> (C=O) amide I
1701	H-bonded <i>n</i> (C=O) amide I
1598	<i>n</i> pyridine ring
1595	<i>n</i> aromatic ring
1578	<i>n</i> pyridine ring
1539	H-bonded <i>n</i> (C-N) + <i>d</i> (N-H) amide II
1530	free <i>n</i> (C-N) + <i>d</i> (N-H) amide II
1235	H-bonded <i>n</i> (C-N) + <i>d</i> (N-H) amide III
1202	free <i>n</i> (C-N) + <i>d</i> (N-H) amide III
1106	<i>n</i> (C-O-C)

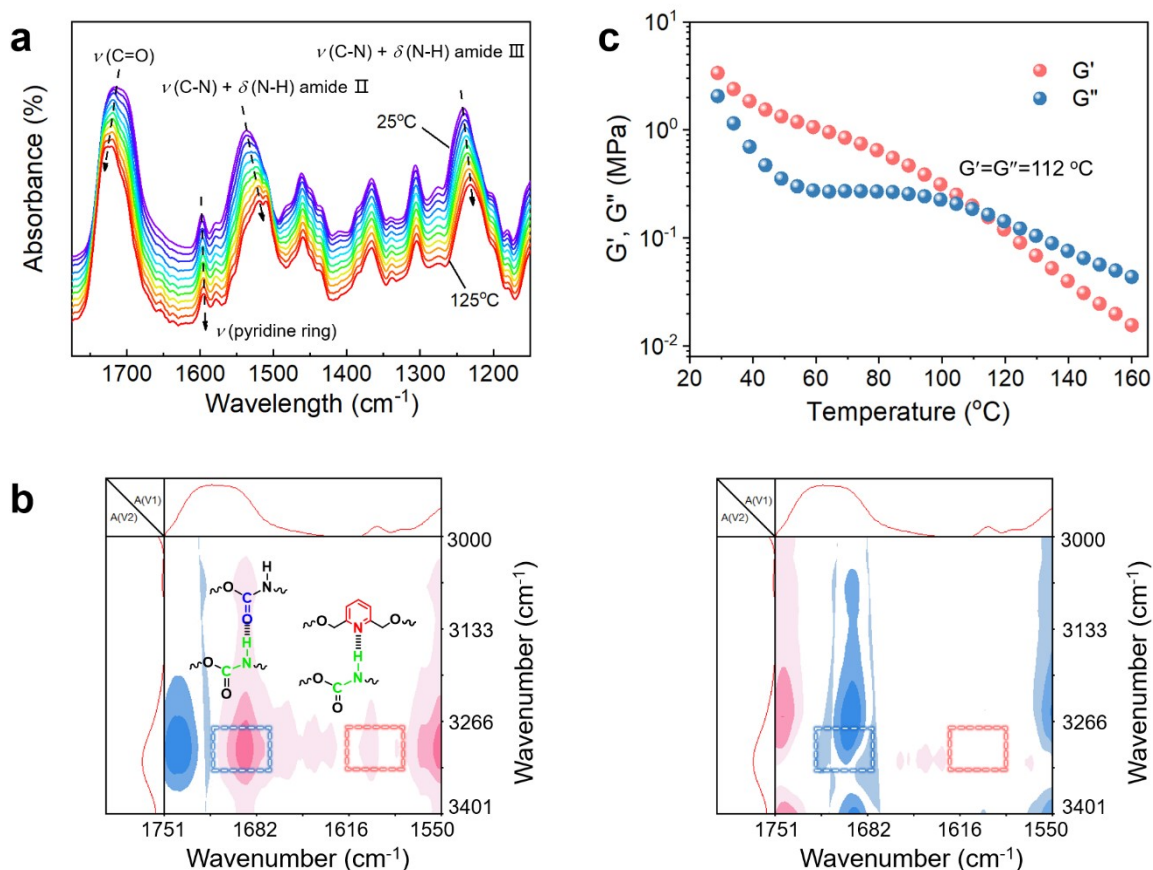


Fig. S3 Characterization of the hierarchical hydrogen bonds in PUPDM. (a) Temperature-dependent Fourier transform infrared spectrum of pristine PUPDM in the temperature range from 25 °C to 125 °C. (b) Synchronous (left) and asynchronous (right) two-dimensional Fourier transform infrared images of pristine PUPDM. (c) Storage shear modulus (G') and loss shear modulus (G'') of pristine PUPDM at different temperatures.

Temperature-dependent Fourier transform infrared spectrum shows an apparent chemical shift of the H-bonding related groups as the temperature increases from 25 °C to 125 °C, proving the disassociation of more hydrogen bonds at an elevated temperature and the reversibility of association/dissociation. In two-dimensional correlated FTIR spectroscopy (2D-FTIR), two correlation cross peaks at ϕ (1701 and 3324) and ϕ (1598 and 3324) can be observed in the synchronous spectrum and then vanish in the corresponding asynchronous spectrum, further accounting for its temperature-dependent nature.

The rheological temperature sweep curve shows that the moduli drop as temperature get higher, validating dynamic H-bonds are dissociated with temperature increasing to afford a thermoplastic property. Meanwhile, G' and G'' have an intersection point at 112 °C, which indicates the transformation from an elastic state to a liquid-like behavior, implying this PUPDM can be used as a hot-melt adhesive.

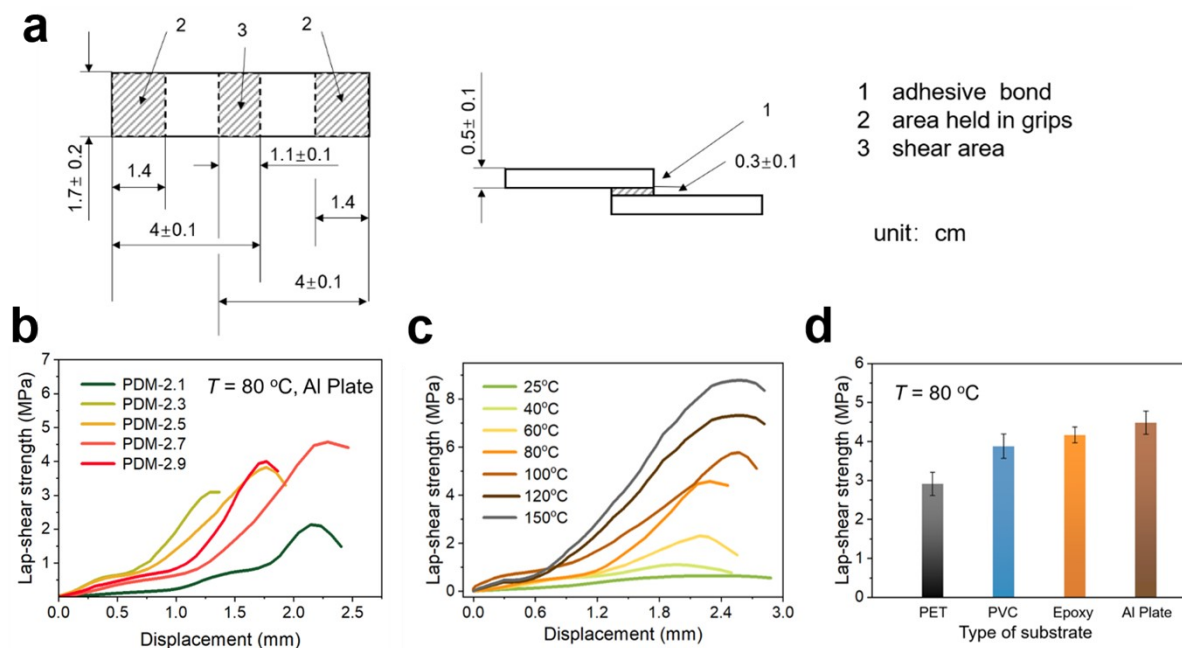


Fig. S4 Lap-shear characterization to qualify the adhesive strength of PUPDM. (a) Schematic details to carry out the lap-shear characterization. (b) Lap-shear strength versus displacement curves of pristine PUPDM with different value of NCO/OH between two gluing aluminum plates at the adhesive temperature of 80 °C. (c) Lap-shear strength versus displacement curves of pristine PUPDM between two gluing aluminum plates at different adhesive temperatures. (d) Lap-shear strength of pristine PUPDM between various gluing plates at the adhesive temperature of 80 °C.

The excess molar ratio of NCO ($\text{NCO/OH} > 2$) was designed to alter the total content of the hard segments after the addition of chain extender, PDM, and thus the hard domains to optimize the mechanical and adhesive properties. For instance, the higher the ratio value, the larger-sized hard domains may be generated through carbamate-carbamate and pyridine-carbamate H-bonding, enabling more hydrogen bonding moieties to be released at high temperature to provide more active binding sites with the hydron bond acceptor or donor on the sandwiched surfaces. Hence, the adhesive property could be optimized by tuning the value of NCO/OH. The adhesion force of PUPDM with NCO/OH value of 2.7 is the highest.

Table S4 Density information of three components in composites.

Materials	Density (g cm ⁻³)
PUPDM	1.07
Liquid metal	6.44
Aluminum oxide	3.70

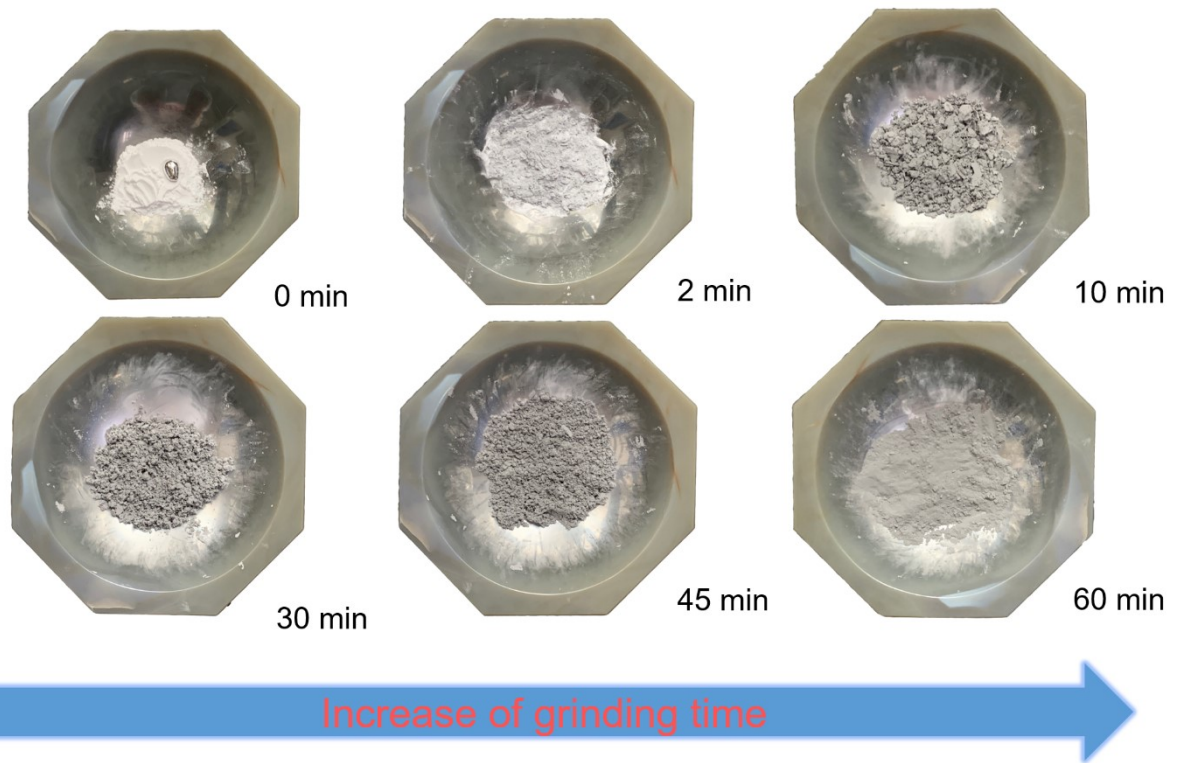


Fig. S5 Preparation of LM/ Al_2O_3 hybrid filler by grinding LM droplet and Al_2O_3 powder for 60 min.

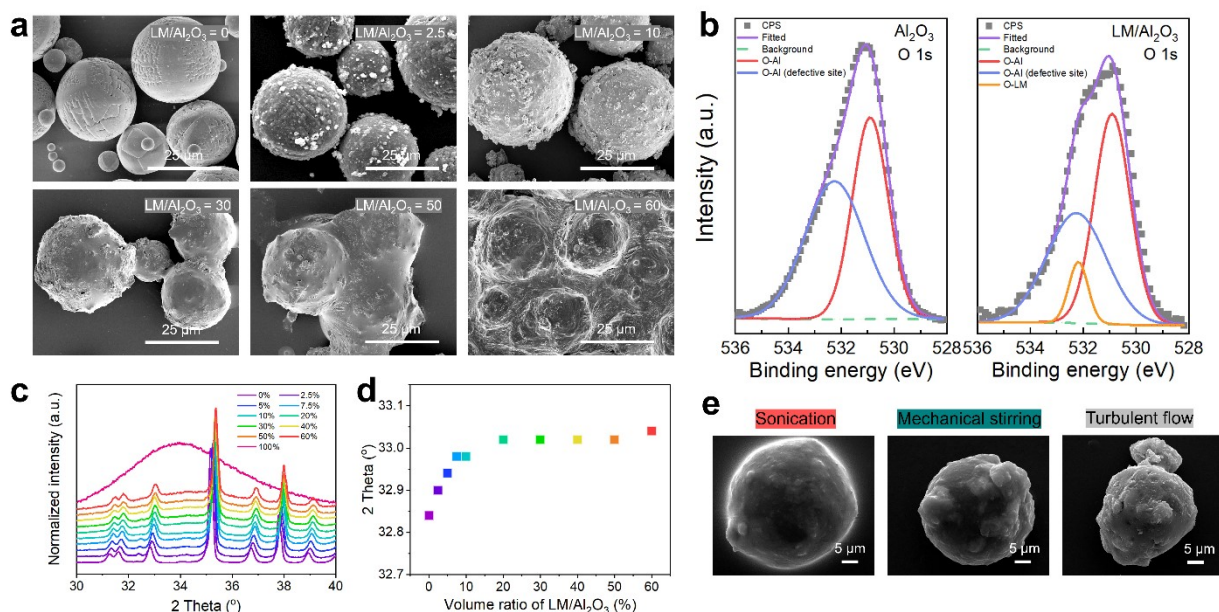


Fig. S6 Characterization of core-shell LM/Al₂O₃. (a) Scanning electron microscopy image of LM/Al₂O₃ with different volume ratios of LM. (b) O 1s spectra of X-ray photoelectron spectrum of Al₂O₃ and LM/Al₂O₃. (c) X-ray diffraction result of LM/Al₂O₃ and (d) its characteristic peak position as an increase of the volume ratio (LM: Al₂O₃). (e) Scanning electron microscopy images of the hybrid filler after 15 min treatment by ultrasonication, mechanical stirring and turbulent flow.

According to scanning electron microscopy image of LM/Al₂O₃, as the volume ratio of LM to Al₂O₃ increases gradually, there are three kinds of morphological characteristics of LM droplets on the surface of spherical aluminum oxide and they are respectively are partial coating, full coating and over coating according to the coating type.

X-ray photoelectron spectroscopy (XPS) spectrum shows, compared with the O_{1s} peak of the pristine Al₂O₃, the O_{1s} peak of the LM/Al₂O₃ hybrid filler can be deconvoluted an additional peak (at 532.2 eV) which confirms the presence of the possible coordination bonds between LM and Al₂O₃ besides the peak at 530.9 eV and 532.3 eV respectively corresponding to oxygen atoms in the oxide lattice (O²⁻) of aluminum oxide and oxygen atoms near vacancy-type defects in the oxide.

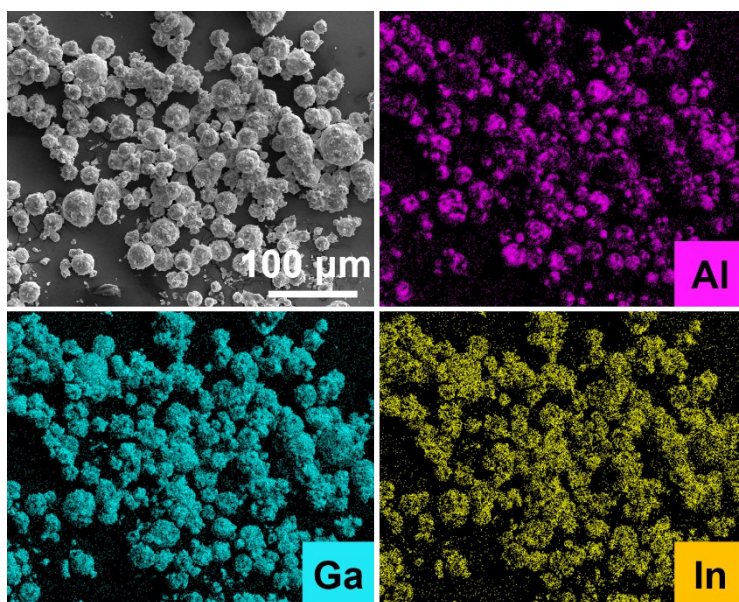


Fig. S7 Scanning electronic microscopy mapping results of LM/Al₂O₃ filler with magnification of 250 manifest its core-shell morphology.

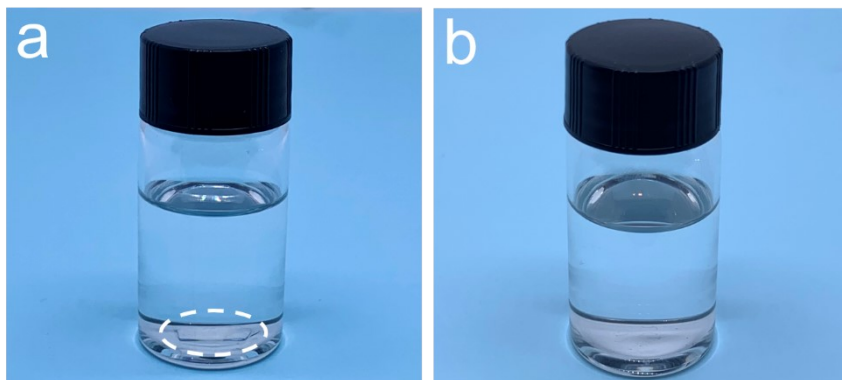


Fig. S8 Dissolution test of PUPDM in THF.

It could be found clearly that PUPDM could be dissolved in THF completely, proving it is not crosslinked.

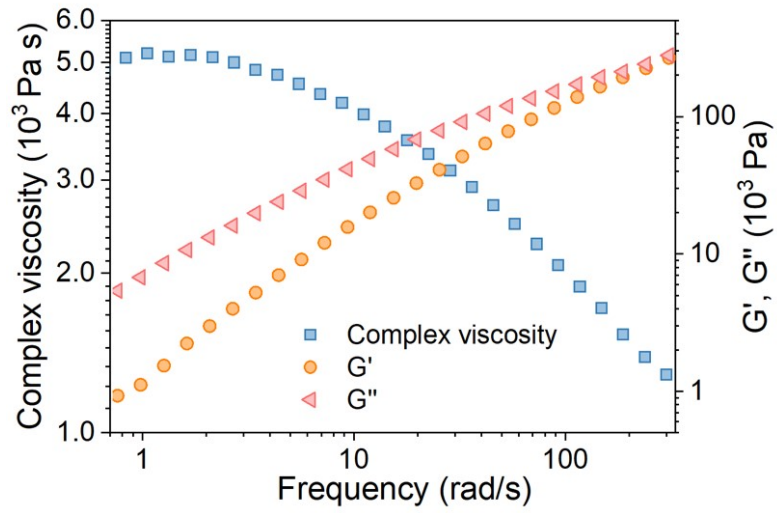


Fig. S9 Variation in storage shear modulus (G'), loss shear modulus (G'') and complex viscosity of the PUPDM as a function of angular frequencies (ω) at 170 °C.

It is clear to see Newtonian-like terminal region for viscosity and slope of 1 and 2 for G'' and G' at low frequency region in frequency sweep at 170 °C, suggesting that PUPDM is thermoplastic and not fully crosslinked.

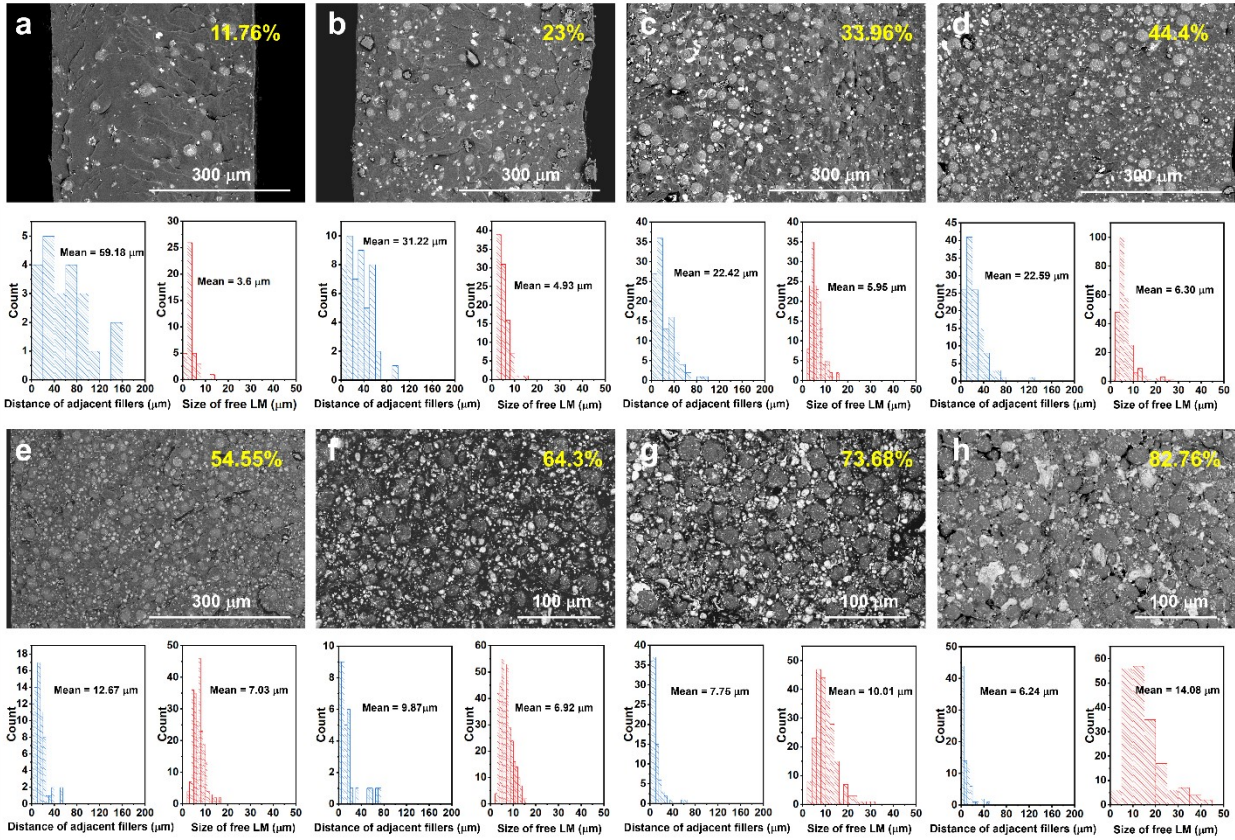


Fig. S10 Statistics of the distance of adjacent fillers and the size of free LM droplets. (a-h) Scanning electron microscopy images of the PUPDM/LM/Al₂O₃ composites at the different binary filler contents and the volume ratio of LM: Al₂O₃ is 30%. (Note that we use electron backscatter diffractometer (EBSD) to obtain the following SEM images in which the brighter region represents higher ordinal element. Hence, the white regions are LM. The light grey regions are spherical aluminum oxide and the dark grey regions are PUPDM matrix.)

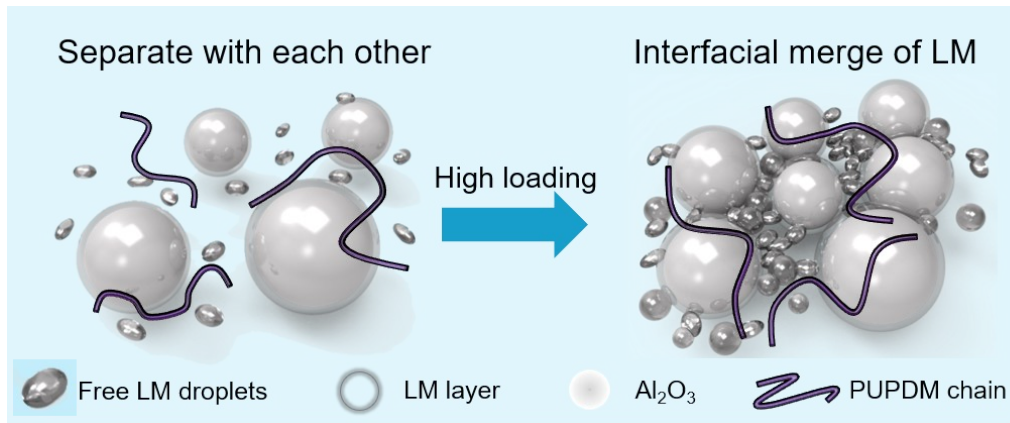


Fig. S11 Schematic of the PUPDM/LM/Al₂O₃ composites at a low and a high filler loading, showing the bridge effect of LM.

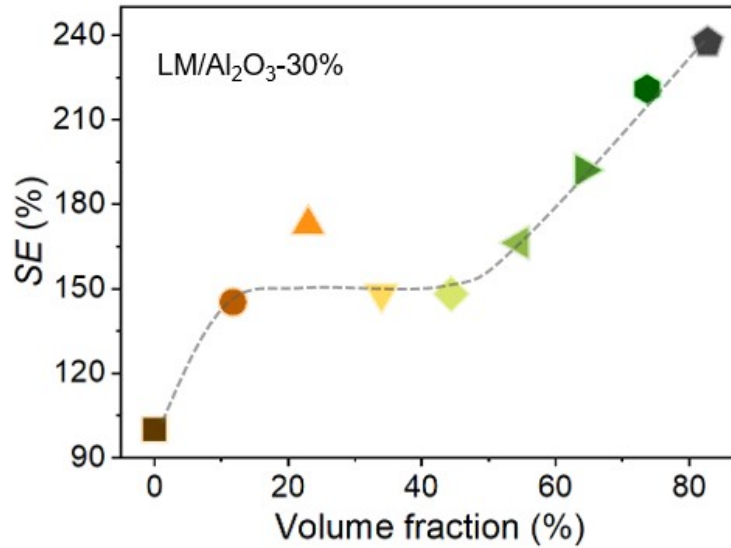


Fig. S12 Synergistic efficiency as a function of the volume fraction of LM/Al₂O₃ binary filler in the PUPDM/LM/Al₂O₃ composites. Noted that the volume ratio of LM: Al₂O₃ is 30%.

The synergistic efficiency (*SE*) represents the synergy between LM and Al₂O₃ on the thermal conductivity of the PUPDM/LM/Al₂O₃ composites, defined as the following equation:

$$SE = \frac{\lambda_{LM/Al_2O_3} - \lambda_{PU}}{(\lambda_{LM} - \lambda_{PU}) + (\lambda_{Al_2O_3} - \lambda_{PU})}$$

where the λ_{LM/Al_2O_3} , λ_{LM} , $\lambda_{Al_2O_3}$ and λ_{PUPDM} represent the thermal conductivity of PUPDM/LM/Al₂O₃, PUPDM/LM, PUPDM/Al₂O₃ and PUPDM, respectively. If the value of *SE* is greater than 1, it indicates that LM and Al₂O₃ exhibit a good synergistic effect on enhancing the thermal conductivity of the PUPDM composite. Moreover, the higher the value of *SE*, the stronger the synergistic effect of the binary filler.

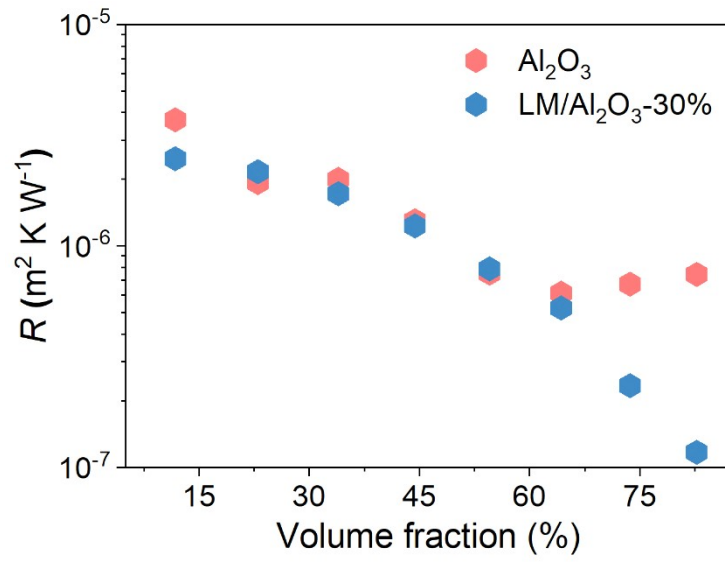


Fig. S13 Average thermal interfacial resistance (R) as a function of the volume fraction of the binary fillers

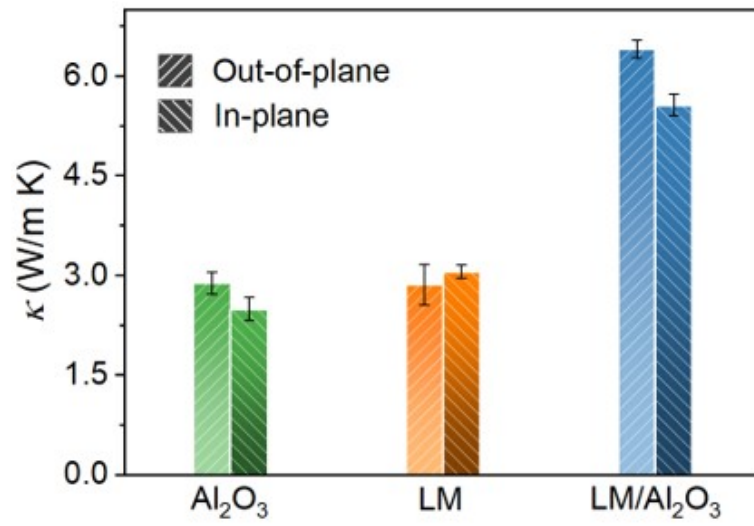


Fig. S14 Out-of-plane and in-plane thermal conductivity of the PUPDM composite involving the different 82.76 vol% filler.

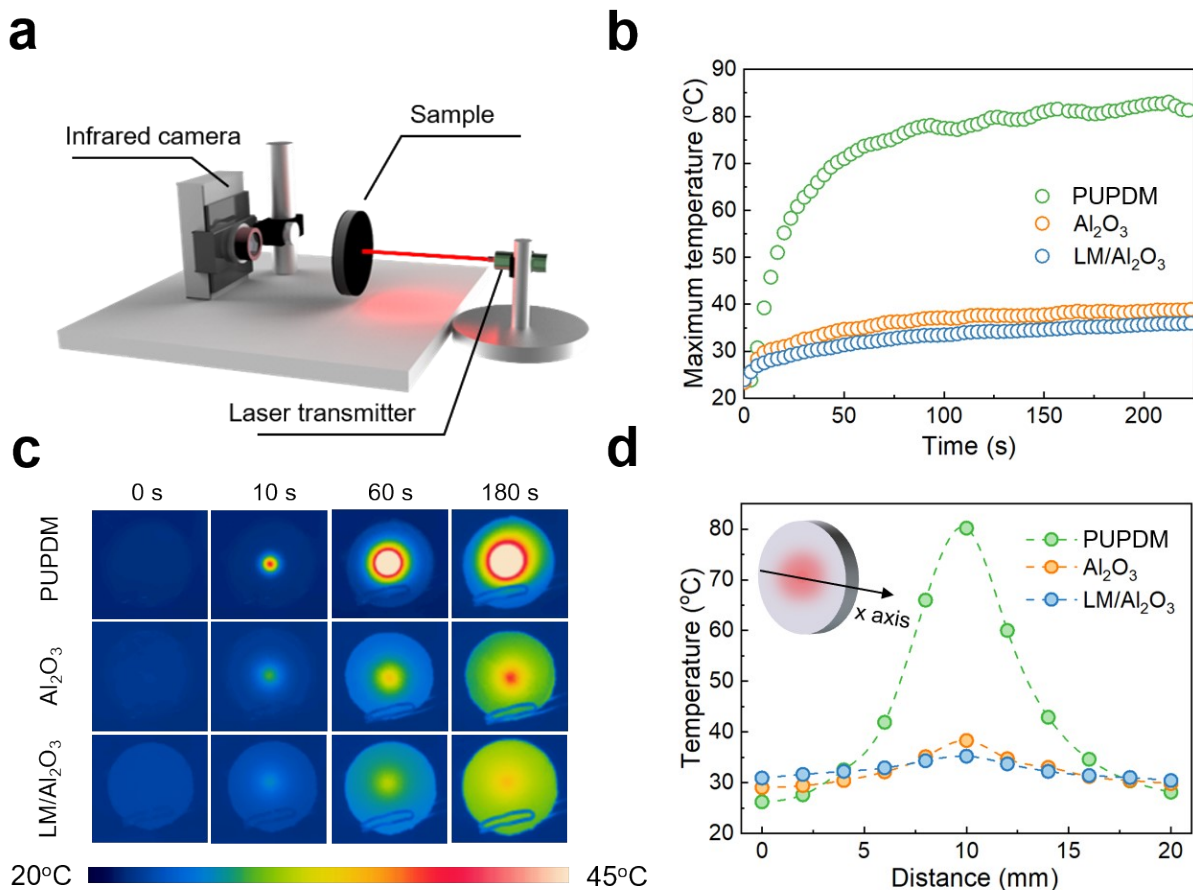


Fig. S15 The thermal management of a spot-like heat source. (a) Schematic illustration of a laser-infrared thermal imaging experiment. (b) The maximum surface temperature evolution of PUPDM, PUPDM/Al₂O₃ and PUPDM/LM/Al₂O₃ as a function of the heating time. (c) Infrared camera images as a function of heating time by a localized heat source, and (d) their 180 s-temperature distributions on the surface of the different PUPDM composite samples.

We applied a localized heat source (powered by a laser transmitter) on one surface of the samples (Fig. S11a). Their external surface was sprayed with graphite to guarantee the identical absorption of laser energy. The temperature and infrared images were recorded according to another surface as a function of time. Compared with the pristine PUPDM and PUPDM/Al₂O₃ counterpart, the heat dissipates significantly because the hot spot on the PUPDM/LM/Al₂O₃ sample exhibits the minimum temperature (Fig. S11b). Moreover, its temperature distribution is very uniform (Fig. S11c, d) compared to PUPDM, and PUPDM/Al₂O₃ samples, due to the faster and isotropic thermo-conductive property in the PUPDM/LM/Al₂O₃ composite contributes to the multi-directional heat flux.

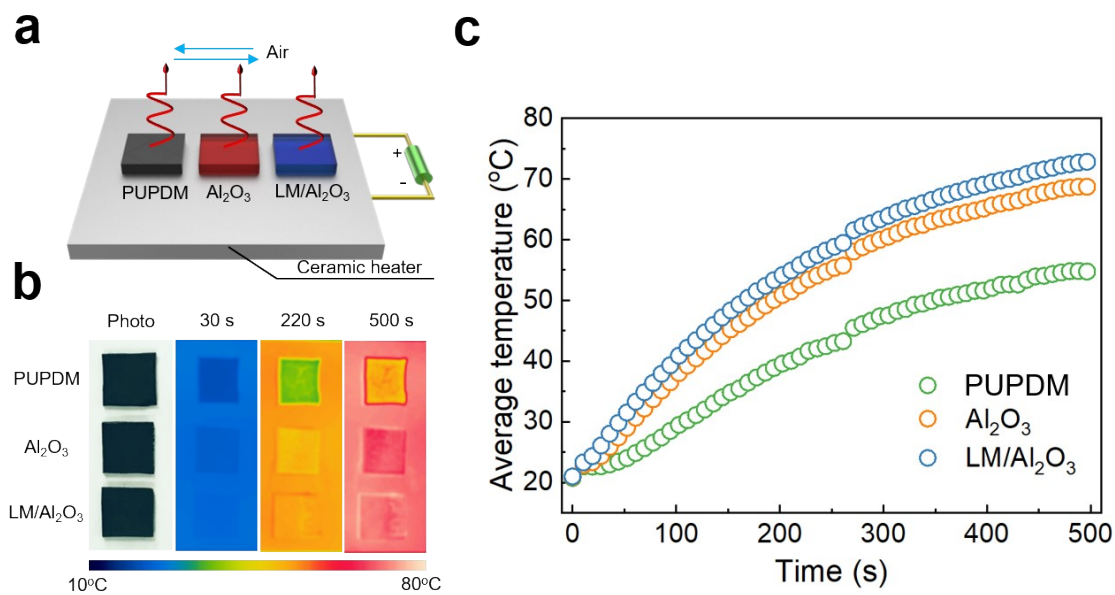


Fig. S16 The thermal management of a large-area heat source. (a) Schematic illustration of a large heat source simulated by putting samples on a ceramic heater. (b) Infrared camera recorded images and (c) the corresponding surface temperature evolution of PUPDM, PUPDM/Al₂O₃ and PUPDM/LM/Al₂O₃ as a function of the heating time.

Three samples cut into the size of 10 mm × 10 mm × 1 mm were placed on the surface of a ceramic heater (10W) and kept at room temperature in the beginning, followed by heating simultaneously. We found that the surface temperature of PUPDM/LM/Al₂O₃ increases faster than that of the other two samples and always exhibits the higher value, for example, the average temperature of PUPDM, PUPDM/Al₂O₃ and PUPDM/LM/Al₂O₃ at 500 s is 55 °C, 69 °C and 73 °C, respectively. Therefore, PUPDM/LM/Al₂O₃ sample manifested the most rapid through-plane heat conduction.

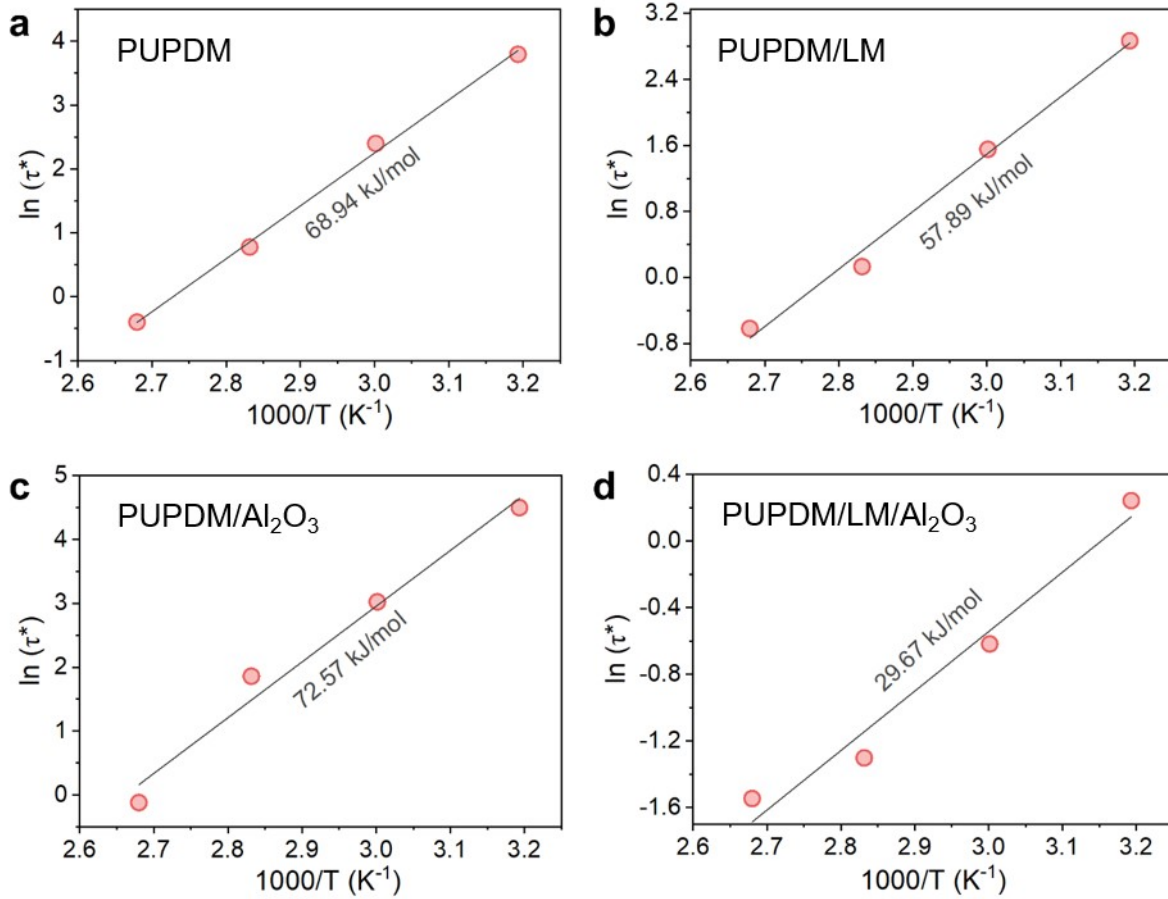


Fig. S17 Arrhenius plots at the different temperatures and the activation energy calculated from the linear fit slope of the Arrhenius plots of (a) PUPDM, (b) PUPDM/LM, (c) PUPDM/Al₂O₃ and (d) PUPDM/LM/Al₂O₃.

The activation energy (E_a) is calculated by Arrhenius equation:

$$\tau(T) = \tau_0 e^{\left(\frac{E_a}{RT}\right)}$$

where $\tau(T)$ is the stress relaxation time at temperature T (K), τ_0 is a constant, E_a is the relaxation activation energy and R is the ideal gas constant. $\tau(T)$ can be directly deduced from the following equation with reference to relaxation curves:

$$\sigma = \sigma_0 e^{(-t/\tau)}$$

where σ_0 (MPa) is the initial stress, σ is the real-time stress at time t (s) and the relaxation time τ_c is determined as the time when $\sigma/\sigma_0=1/e$.

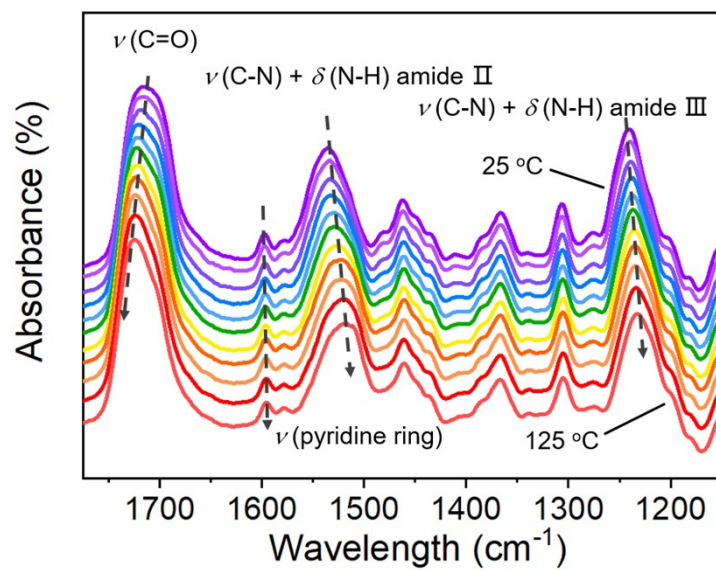


Fig. S18 Temperature-dependent Fourier transform infrared spectrum of the PUPDM/LM/Al₂O₃ in the temperature range from 25 °C to 125 °C.

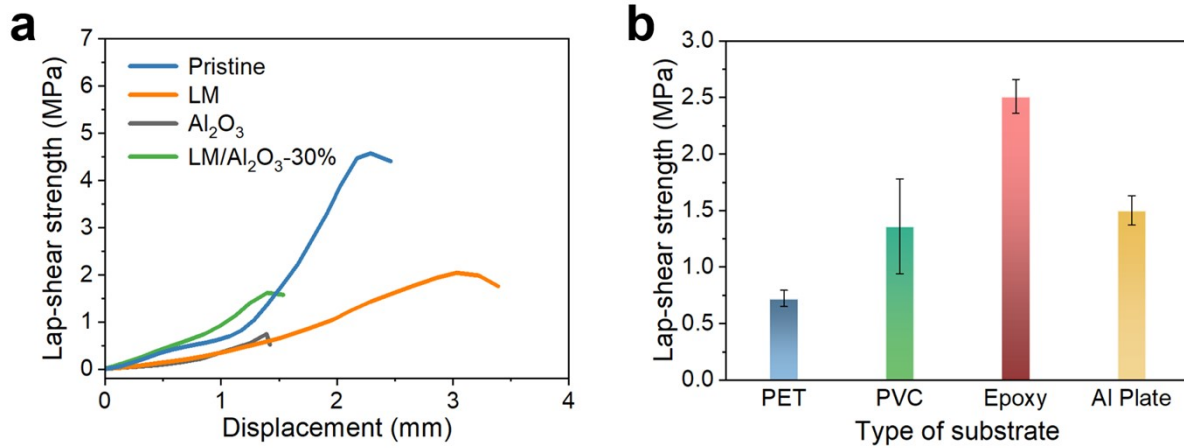


Fig. S19 Lap-shear strength of PUPDM composites (a) Lap-shear strength versus displacement curves of PUPDM, PUPDM/Al₂O₃, PUPDM/LM and PUPDM/LM/Al₂O₃ in gluing aluminum plates at 80 °C. (b) Lap-shear strength of the PUPDM/LM/Al₂O₃ composites in gluing different substrates at 80 °C.

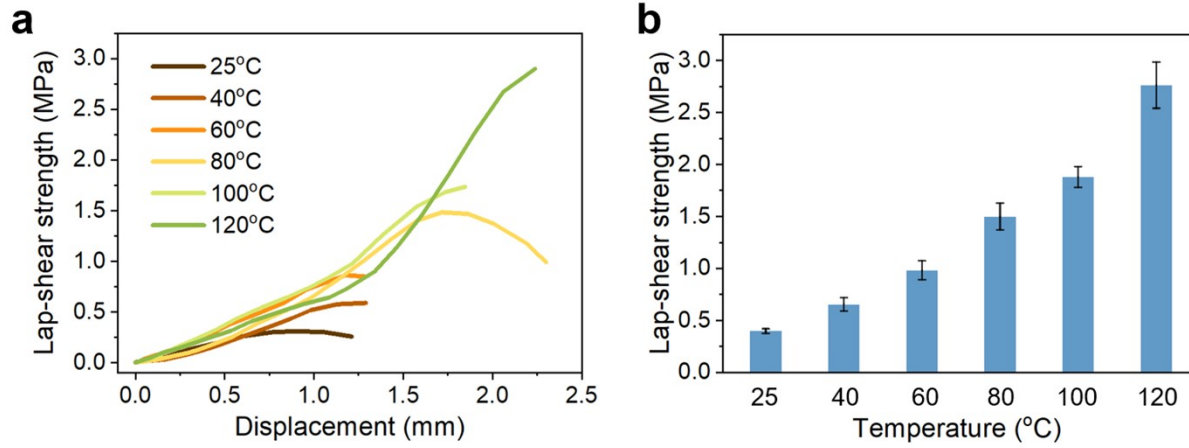


Fig. S20 Temperature dependence of lap-shear strength of PUPDM/LM/Al₂O₃ composite (a) Lap-shear strength versus displacement curves of the PUPDM/LM/Al₂O₃ composites in gluing aluminum plates at different temperatures. (b) Lap-shear strength of the PUPDM/LM/Al₂O₃ composites in gluing aluminum plates at different temperatures.

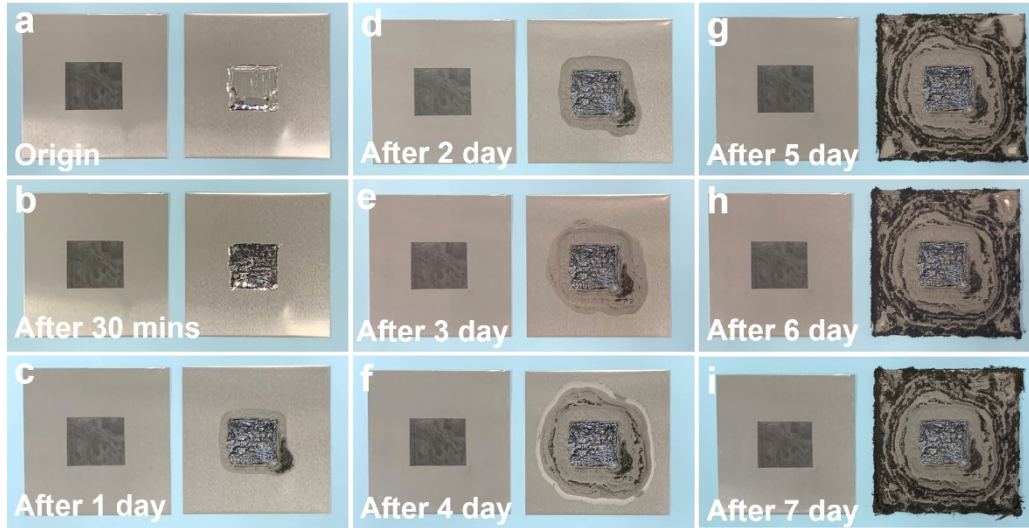


Fig. S21 Corrosion of aluminum surface after contacting with PUPDM/LM/ Al_2O_3 and LM verse time.

As shown in Fig. S19, liquid metal and PUPDM/LM/ Al_2O_3 composite were put on the two pieces of aluminum at the same time to verify the anticorrosion characteristics of our composite. It can be found that the aluminum coated with PUPDM/LM/ Al_2O_3 composite remains clean as its original state after 7 days, whereas the aluminum coated with LM has been corroded severely.

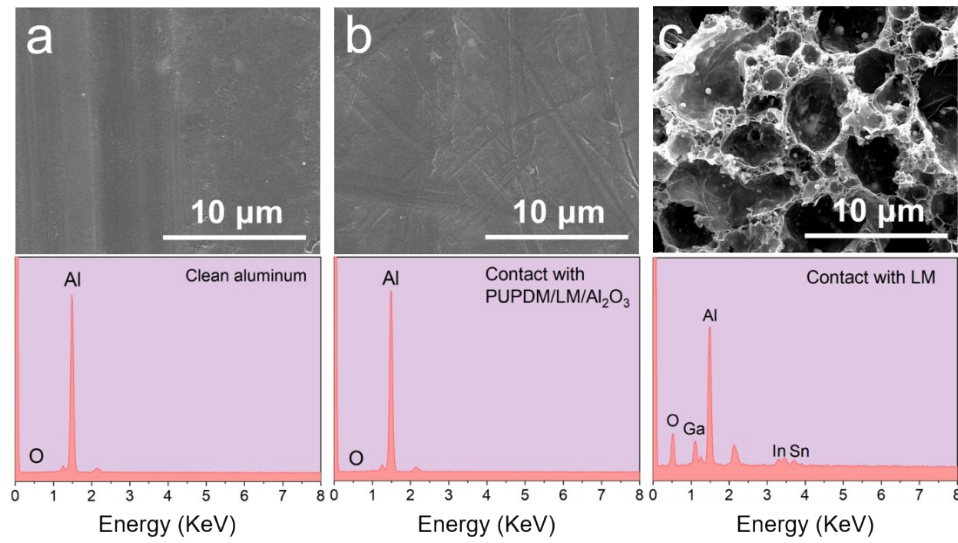


Fig. S22 SEM images and energy-dispersive spectra results of (a) clean aluminum, (b) aluminum surface after contacting with PUPDM/LM/Al₂O₃ for a week and (c) aluminum surface after contacting with LM for a week.

The aluminum surface after contacting with LM for a week became rough and porous. The increasement of oxygen and gallium elements and the relative reduction of aluminum could further demonstrate the original aluminum had been corroded completely. However, after contact with PUPDM/LM/Al₂O₃ for a week, the aluminum surface did not have any changes of morphology and elemental composition compared to the clean aluminum, indicating no reaction between aluminum and gallium in our composite.

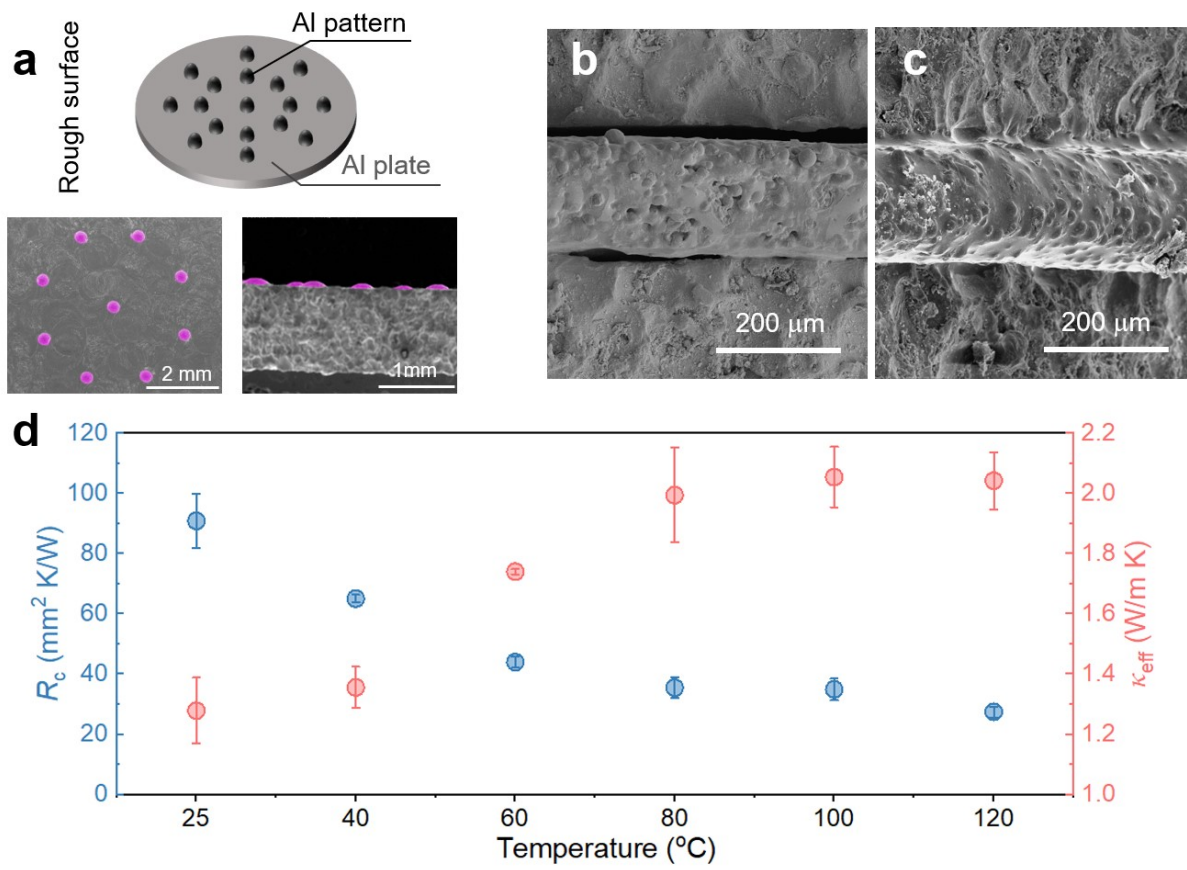


Fig. S23 Interfacial thermal management for rough substrates (a) Schematic illustration describes the configuration of the rough aluminum plate and its morphologies from the top view and the main view. (b) Scanning electronic microscopy images of the microscopic interface between the PUPDM/LM/Al₂O₃ composite and the rough aluminum plates when adhered at 25 and 80 °C, respectively. (c) Thermal contact resistance and the effective thermal conductivity of the PUPDM/LM/Al₂O₃ composite TIM as a function of the adhered temperature in the sandwiched rough aluminum plates.

The thickness of aluminum plate is 1 mm and the patterns designed as humps with diameter of 0.4 mm and height of 0.1 mm were processed by CNC milling machine. A number of gaps or voids could be observed distinctly in the cross-sectional SEM images when the adhesion temperature is 25 °C but disappear at 80 °C. Similarly, the variation of R_c shows a downtrend and its minimum value could approach 27.50 mm² K/W. κ_{eff} of TIM is enhanced as the adhesion temperature increases owing to the improvement of the dual factors-compressibility and adhesion force.

Table S5 Comparison of thermal contact resistance (two sides) of PUPDM/LM/Al₂O₃ composite TIM with those of reported TIMs.

Interfaces	Measurement pressure [KPa]	Thermal contact resistance [mm ² K/W]	Ref.
This Work			
Al/PUPDM-LM-Al ₂ O ₃ /Al	0	18.28	
Reported TIMs			
Al/CNT buckypaper/Al	275.8	81	1
Al/CNT buckypaper with silicon oil/Al	275.8	35	1
Ceramic/Graphene monolith/Cu	81/308/500	20.2/6.0/5.8	2
Ceramic/Thermal pad (5000S35,250 μm)/Cu	517.1	69	3
Ceramic/Graphene-SiC hybrid paper/Cu	517.1	47	3
Ceramic/Thermal pad (5000S35,100 μm)/Cu	413.7	63.3	4
Ceramic/Vertically aligned graphene nanowalls/Cu	413.7	23.7	4
Ceramic/Thermal pad (5000S35,400 μm)/Cu	325	62.9	5
Ceramic/Graphene paper/Cu	325	17.8	5
Cu/VACNT/Cu	217.7/439.4	30.51/19.54	6
Al/Vertically aligned graphene monolith/Al	9000	66	7
Al/Au-vertically aligned graphene monolith-Au/Al	9000	41	7
Cu/MWCNT-nano Cu-epoxy/Cu	1000	60	8
Cu/MWCNT-epoxy/Cu	1000	31.1	8

References

1. H. Chen, M. Chen, J. Di, G. Xu, H. Li and Q. Li, *J. Phys. Chem. C*, 2012, **116**, 3903-3909.
2. W. Dai, T. Ma, Q. Yan, J. Gao, X. Tan, L. Lv, H. Hou, Q. Wei, J. Yu and J. Wu, *ACS Nano*, 2019, **13**, 11561-11571.
3. W. Dai, L. Lv, J. Lu, H. Hou, Q. Yan, F. E. Alam, Y. Li, X. Zeng, J. Yu, Q. Wei, X. Xu, J. Wu, N. Jiang, S. Du, R. Sun, J. Xu, C.-P. Wong and C.-T. Lin, *ACS Nano*, 2019, **13**, 1547-1554
4. Q. Yan, F. E. Alam, J. Gao, W. Dai, X. Tan, L. Lv, J. Wang, H. Zhang, D. Chen and K. Nishimura, *Adv. Funct. Mater.*, 2021, **31**, 2104062.
5. J. Gao, Q. Yan, L. Lv, X. Tan, J. Ying, K. Yang, J. Yu, S. Du, Q. Wei, R. Xiang, Y. Yao, X. Zeng, R. Sun, C.-P. Wong, N. Jiang, C.-T. Lin and W. Dai, *Chem. Eng. J.*, 2021, **419**, 129609.
6. L. Ping, P.-X. Hou, H. Wang, M. Chen, Y. Zhao, H. Cong, C. Liu and H.-M. Cheng, *Carbon*, 2018, **133**, 275-282.
7. X. Tan, J. Ying, J. Gao, Q. Yan, L. Lv, K. Nishimura, Q. Wei, H. Li, S. Du, B. Wu, R. Xiang, J. Yu, N. Jiang, C.-T. Lin and W. Dai, *Compos. Commun.*, 2021, **24**, 100621.
8. P. Zhang, Q. Li and Y. Xuan, *Compos. Part A: Appl. Sci. Manuf.*, 2014, **57**, 1-7.